Electronic Supplementary Material (ESI) for Journal of Materials Chemistry A.

Amorphous C/SbS$_x$ composite from natural stibnite as low cost and high performance lithium/sodium-ion battery anodes

Shuonan Wang,[a] Yao Hao,[b,c] Kai Zhang,[c] Hao Liu*[b] and Libing Liao*[a]

[a] Engineering Research Center of Ministry of Education for Geological Carbon Storage and Low Carbon Utilization of Resources, School of Material Sciences and Technology, China University of Geosciences (Beijing), Beijing 100083, China. Email: LiBing Liao, clayl@cugb.edu.cn.

[b] School of Science, China University of Geosciences, Beijing 100083, China. Email: Hao Liu, liuhao1398@cugb.edu.cn.

[c] Beijing Synchrotron Radiation Facility Institute of High Energy Physics, Chinese Academy of Science, Beijing 100049, China.

Supplementary text:

Video S1 shows the microwave process of preparing the C/SbS_x-MW-1:2 composite. The sample heats up rapidly and emits red light during the microwave process. As the heat transfer causes the crucible to warm up, but the slow cooling rate of the crucible causes the cooling rate of the sample near the crucible wall to become slow, eventually producing a crystalline C/Sb_2S_3 composite. Due to the difference in cooling rate between the center and the edge of the crucible, the final product exhibited a distinct separation. The samples at the center and the edge of the crucible cannot be completely separated. To increase the yield, some samples from the edge of the crucible will be mixed when sieving the samples from the center. Without considering the yield, samples with a higher proportion of amorphous can be obtained from the center of the crucible. In this paper, the focus is on the amorphous composite in the crucible center.

Figure S1. Optical photograph of the natural stibnite.

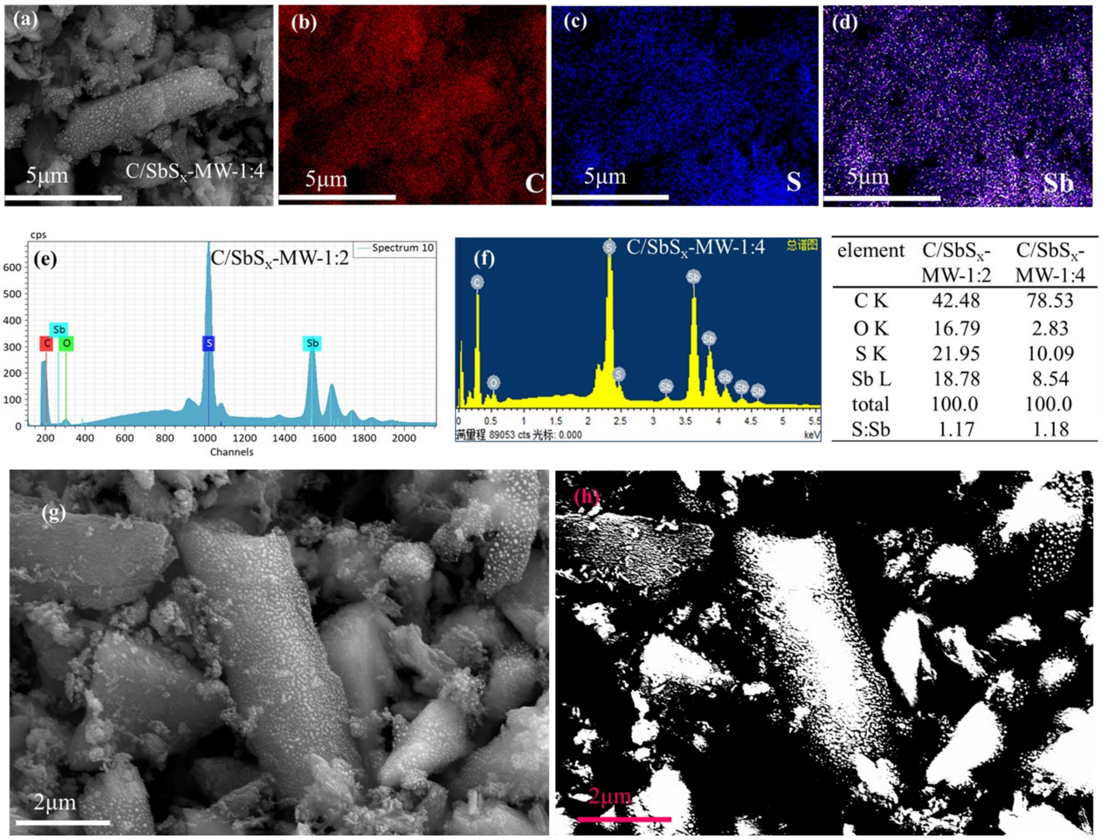

element	C/SbS$_x$-MW-1:2	C/SbS$_x$-MW-1:4
C K	42.48	78.53
O K	16.79	2.83
S K	21.95	10.09
Sb L	18.78	8.54
total	100.0	100.0
S:Sb	1.17	1.18

Figure S2. Morphology analyses for C/SbS$_x$-MW-1:4 composite. (a) SEM images and (b-d) EDS mapping of C/SbS$_x$-MW-1:4; EDS spectrum of (e) C/SbS$_x$-MW-1:2 and (f) C/SbS$_x$-MW-1:4. (g) SEM image and (h)corresponding backscattered electron image of C/SbS$_x$-MW-1:4 composite.

As shown in Figure S2a-d, the distribution of Sb, S, and C elements in C/SbS$_x$-MW-1:4 composite is consistent, representing the successful synthesis of C/SbS$_x$-MW-1:4 composite. In the EDS spectrum of C/SbS$_x$-MW-1:2 and C/SbS$_x$-MW-1:4, it can be found that the ratio of S to Sb is 1.17-1.18, there are part of S lost during microwave process. As shown in Figure S2g-h, it can be seen that in C/SbS$_x$-MW-1:4, SbS$_x$ is not only distributed on the Pristine matrix, but also may form spherical nanoparticles on the Pristine C surface.

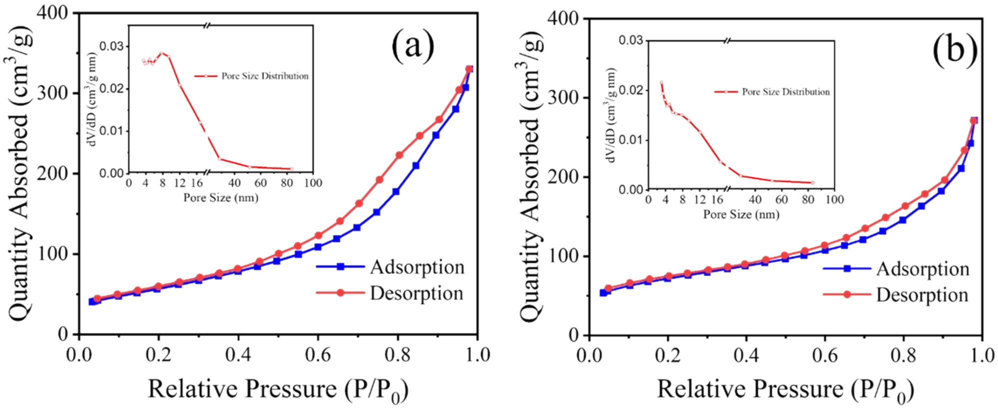

Figure S3. N_2 adsorption-desorption curves of (a) Pristine C and (b)C/SbS_x-MW-1:2.

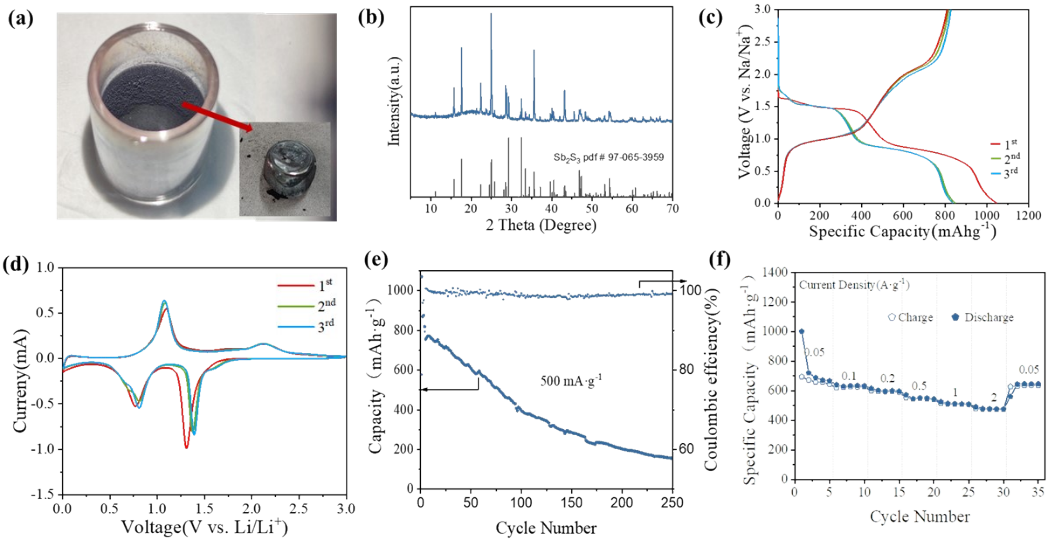

Figure S4. (a) Optical photo, (b) XRD pattern and (c) Galvanostatic discharge/charge profiles, (d) CV curves, (e) Cycling performance and (f) Rate performance of the sample containing crystalline Sb_2S_3 at the edge of the crucible.

As shown in Figure S45a, the crystalline Sb_2S_3 produced adhered to the crucible, forming larger particles. Figure S4b confirmed that the formed Sb_2S_3 had good crystallinity. The discharge plateau at about 1.5V in the Galvanostatic discharge/charge profiles, and the sharp redox peak at 1.4V in the CV curve, were both in the same position as Pristine Sb_2S_3, indicating that most of the components were crystalline Sb_2S_3. As shown in Figure S4e-f, the crystalline Sb_2S_3 had good rate performance, but poor cycle stability.

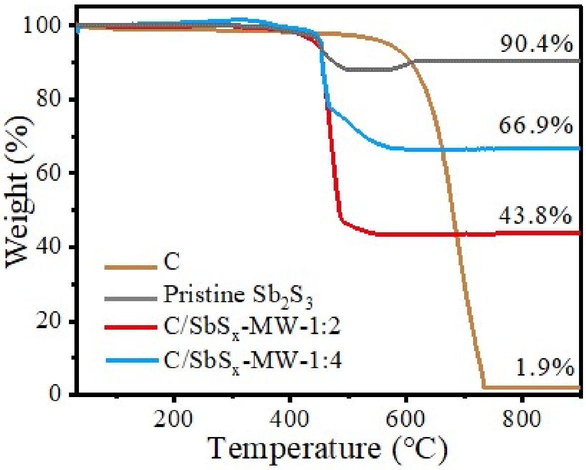

Figure S5. TGA curves of C/SbSx composite.

The 98% weight loss of Pristine C can be observed at about 600-700 °C, which can be ascribed to the combustion of carbon. For Pristine Sb_2S_3, C/SbS_x-MW-1:2 and C/SbS_X-MW-1:4, the 9.6%, 33.1% and 56.5% weight loss at about 450 °C, which is attributed to the oxidation of Sb_2S_3 to Sb_2O_4 and the combustion of carbon.[1-3]

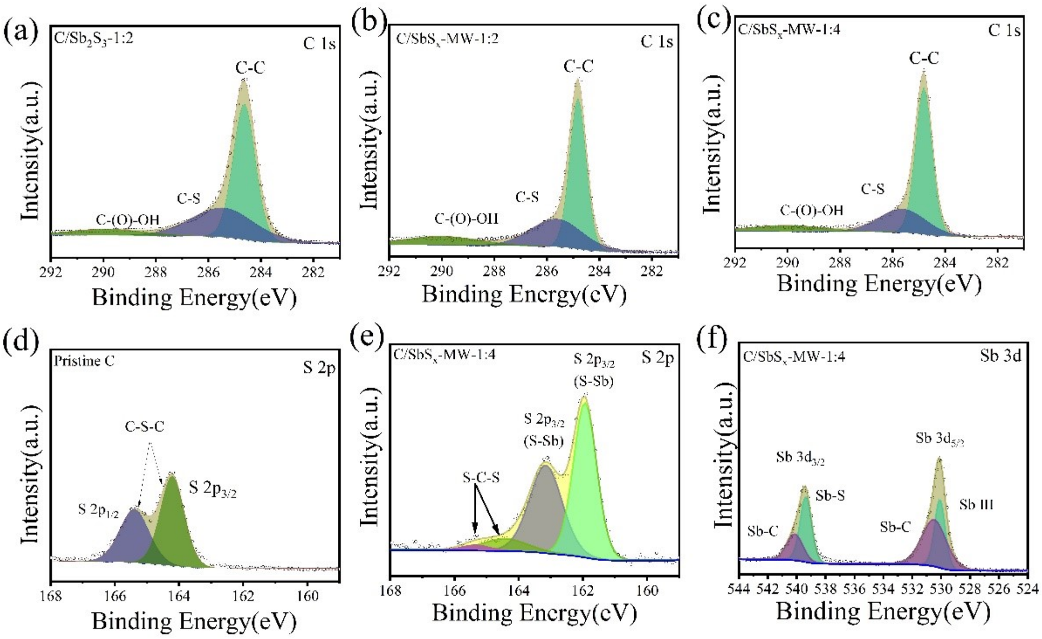

Figure S6. XPS spectra of C/SbS$_x$ composite. C 1s XPS spectra of (a) C/Sb$_2$S$_3$-1:2, (b) C/SbS$_x$-MW-1:2 and (c) C/SbS$_x$-MW-1:4; (d) S 2p XPS spectra of Pristine C; (e) S 2p and (f) Sb 3d XPS spectra of C/SbS$_x$-MW-1:4.

The high-resolution spectrum of C 1s is divided into three peaks, as shown in Figure S6a-c. The strong peak at 284.8 eV is corresponding to conjugated honeycomb lattice of C atoms (C-C).[4] The peak at 285.5 eV is assigned to the C-S bond[1]. The peak of C-(O)-OH bond appeared at 290.1 eV, which is caused by the oxidation of the surface. As shown in Figure S6d, the peaks at 164.3 eV and 165.4 eV of S 2p come from Pristine C. Because natural charcoal contains a small amount of S, resulting in sulfur doping of Pristine C. In Figure S6e, the peak of Sb-S bond is stronger in C/SbS$_x$-MW-1:4 compared to C/SbS$_x$-MW-1:2, due to the increased content of SbS$_x$. As shown in Figure S6f, the Sb-C bond is also formed in C/SbS$_x$-MW-1:4.

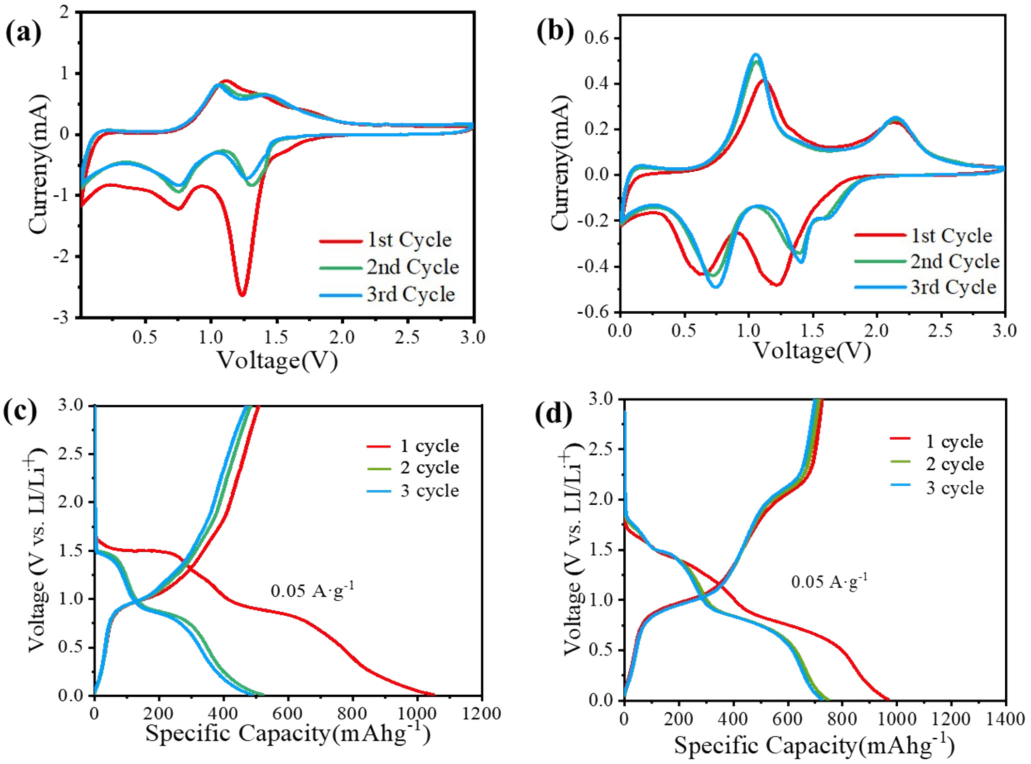

Figure S7. Electrochemical performance of C/Sb_2S_3-1:2 and C/SbS_x-MW-1:4 in LIBs. CV curves of (a) C/Sb_2S_3-1:2, and (b) C/SbS_x-MW-1:4 for the initial three cycles at a scan rate of 0.2 mV·S^{-1}. Galvanostatic discharge/charge profiles of (c) C/Sb_2S_3-1:2, and (d) C/SbS_x-MW-1:4 anodes for the initial three cycles at a current density of 0.05 A·g^{-1}.

For C/Sb_2S_3-1:2 anode, the peak at 1.59 V indicating that the reaction from Sb_2S_3 to Sb and $Li_{0.99}Sb_{5.67}S_9$. And the peak at 1.23 V can be attributed to the reductive of $Li_{0.99}Sb_{5.67}S_9$ to Sb and Li_2S.[5] The peak at 0.8V is assigned to the formation of solid electrolyte interphase (SEI) film and the alloying reaction of forming Li_3Sb between Sb and Li^+.[6] In the anodic scan process, the anodic peak at 1.13V is corresponding to the dealloying process from Li_3Sb to Sb. The followed peak is attributed to the delithiation process of Sb and Li_2S to Sb_2S_3:

Discharge:

$Sb_2S_3 + 0.99Li^+ + 0.99e^- \rightarrow Li_{0.99}Sb_{5.67}S_9 + 0.33Sb$ (1)

$Li_{0.99}Sb_{5.67}S_9 + 17.01Li^+ + 17.01e^- \rightarrow 9Li_2S + 5.67Sb$ (2)

$Sb + 3Li+ + 3e^- \rightarrow Li_3Sb$ (3)

Charge:

$Li_3Sb \rightarrow Sb + 3Li^+ + 3e^-$ (4)

$3Li_2S + 2Sb \rightarrow Sb_2S_3 + 6Li^+ + 6e^-$ (5)

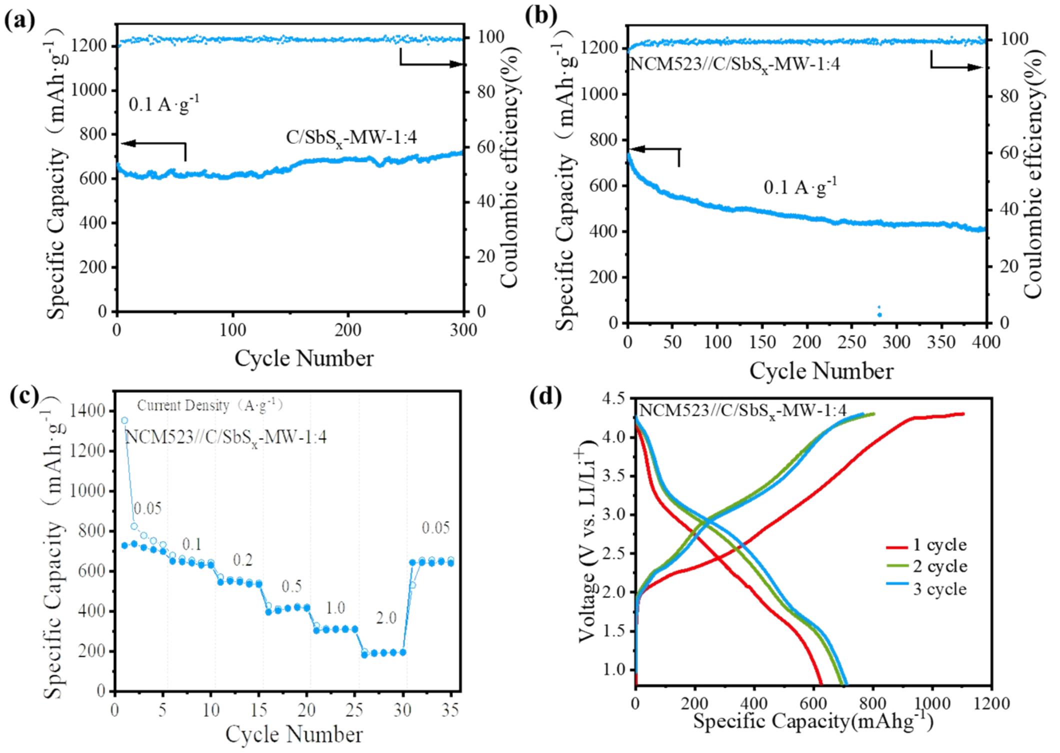

Figure S8. Electrochemical performance of C/SbS_x-MW-1:4 in half-cell and full-cell. (a) Cycling performance of C/SbS_x-MW-1:4 at 0.1 A·g^{-1}. (b) Cycling performance at 0.1A·g^{-1}, (c) Rate performance, (d) Galvanostatic discharge/charge profiles of the NCM523//C/SbS_x-MW-1:4 full cell in the voltage range of 0.8-4.3 V.

As shown in Figure S8a, C/SbS_x-MW-1:4 also shows good cycling stability at a current density of 0.1 A·g^{-1}, with a capacity of 725 mAh·g^{-1} after 300 cycles. In order to detect the electrochemical performance of C/SbS_x-MW-1:4, the mass load of NCM523 cathode is excessive, so the coulombic efficiency is low and the capacity decay is fast in the initial period of cycling. C/SbS_x-MW-1:4 still showed good cycling performance of 408 mAh·g^{-1} after 400 cycles at 0.1 A·g^{-1} (Figure S8b). May be affected by the cathode material, the rate performance is obviously different from that of in half cell. As shown in Figure S8c, the average charge capacity is 773, 657, 552, 420, 316, 196 mAh·g^{-1} at the current densities of 0.05, 0.1, 0.2, 0.5, 1.0, 2.0 A·g^{-1}, respectively. When the current return to 0.05 A·g^{-1}, the discharge capacity is still able to return to 630 mAh·g^{-1}. Due to the excessive NCM523 electrode, the plateaus in the charge-discharge curve of the initial cycle is not obvious, but appears in the second and third cycles (Figure S8d). According to the mass loading of the cathode and anode active materials, the initial N/P ratio was about 0.93. After the first charge/discharge cycle, the N/P ratio quickly dropped to below 0.69 due to the formation of SEI film. The above results demonstrate the good performance of C/SbS_x-MW-1:4 anode in full cell.

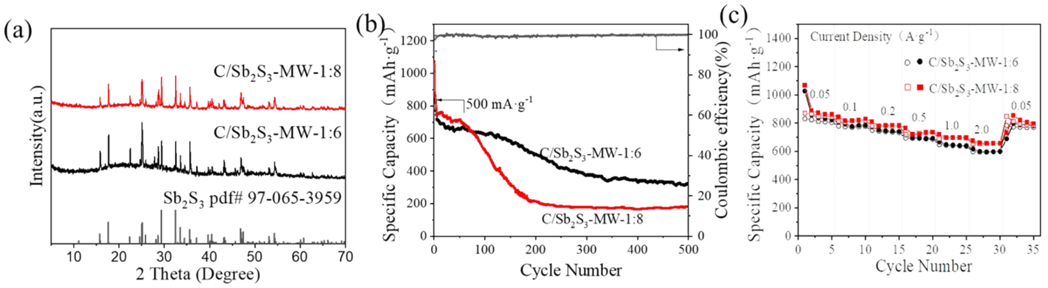

Figure S9. (a) XRD pattern, (b) cycling performance and (c) rate perofrmance of C/Sb_2S_3-MW-1:6 and C/Sb_2S_3-MW-1:8.

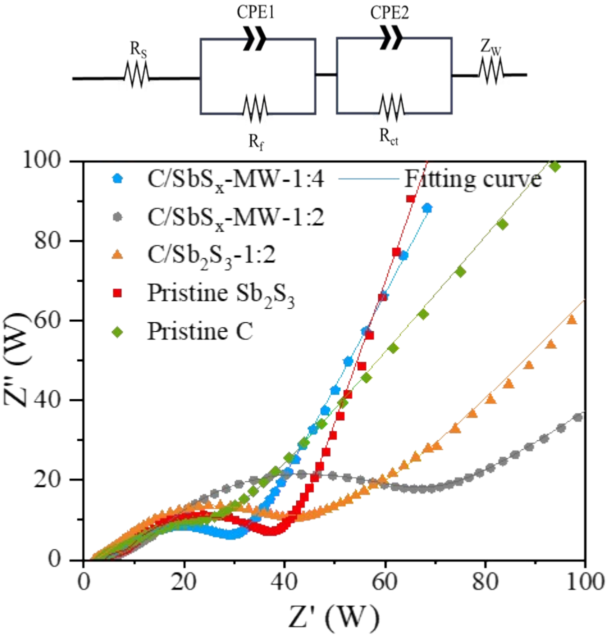

Figure S10. EIS Nyquist plot of Pristine C, Pristine Sb_2S_3, C/Sb_2S_3-1:2, C/SbS_x-MW-1:2, and C/SbS_x-MW-1:4.

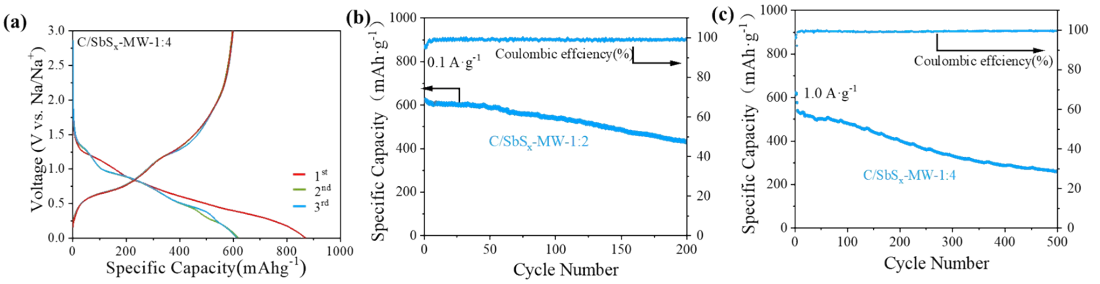

Figure S11. Electrochemical performance of C/SbS$_x$-MW-1:4 composite in SIBs. (a) Galvanostatic discharge/charge profiles of C/SbS$_x$-MW-1:4 electrode for the initial three cycles at a current density of 0.05 A·g^{-1}. Cycling performance of the C/SbS$_x$-MW-1:4 at a current density of (b) 0.1 A·g^{-1} and (c)1.0 A·g^{-1}.

As shown in Figure S11, after 200 cycles at 0.1 mA·g^{-1}, its specific capacity decreased from 608 mAh·g^{-1} to 430 mAh·g^{-1}. After 500 cycles at 1 A/g, its specific capacity decreased from 524 mAh·g^{-1} to 250 mAh·g^{-1}.

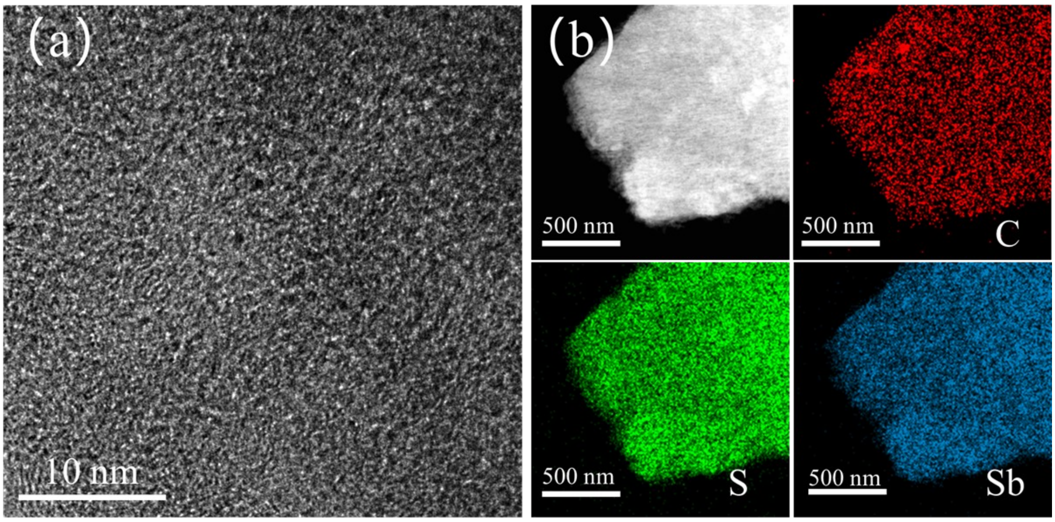

Figure S12. Morphology analyses for C/SbS_x-400℃-1:2. (a) HRTEM image of C/SbS_x-400℃-1:2; (b) HAADF-STEM and corresponding elemental mapping images of C/SbS_x-400℃-1:2.

As shown in Figure S12a, the microstructure of C/SbS_x-400℃-1:2 did not change compared with C/SbS_x-MW-1:2, and the lattice stripes of individual Sb_2S_3 crystals were still not observable, which may be due to the small size of the generated Sb_2S_3 crystals.

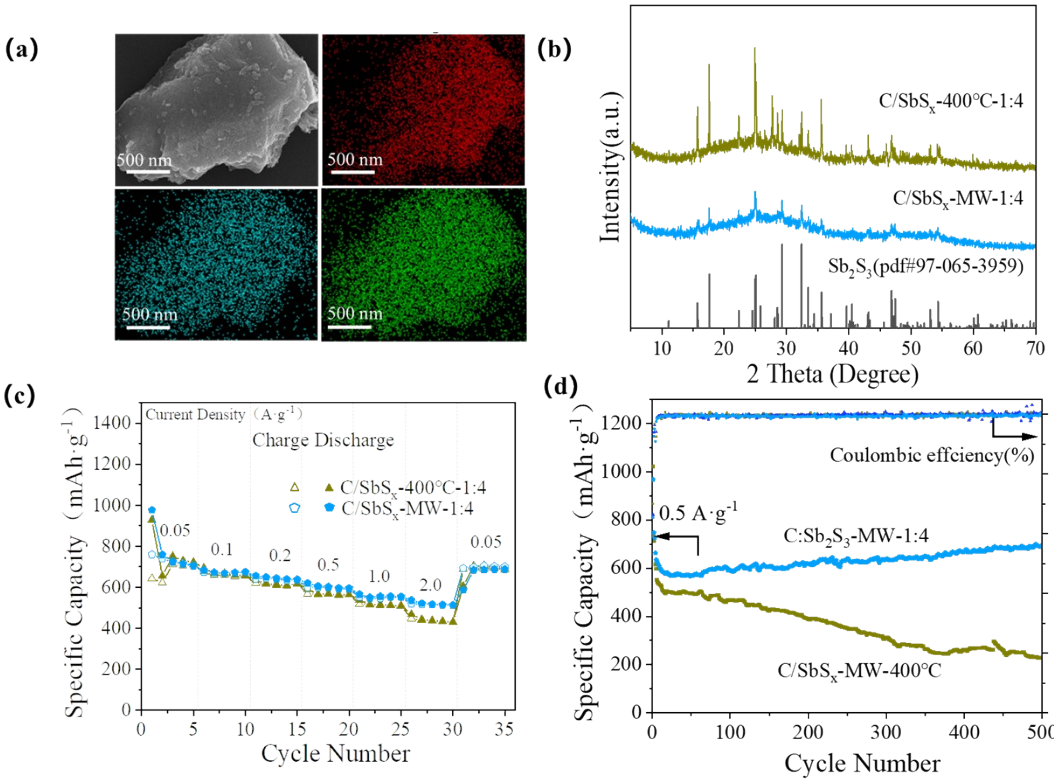

Figure S13. Influence of morphology and crystallinity of C/SbS$_x$-MW-1:4.(a) SEM image EDS mapping of C, Sb, S elements of C/SbS$_x$-400°C-1:4; (b) XRD pattern, (c) rate performance and (d) cycling performance of C/SbS$_x$-MW-1:4 and C/SbS$_x$-400°C-1:4 electrodes.

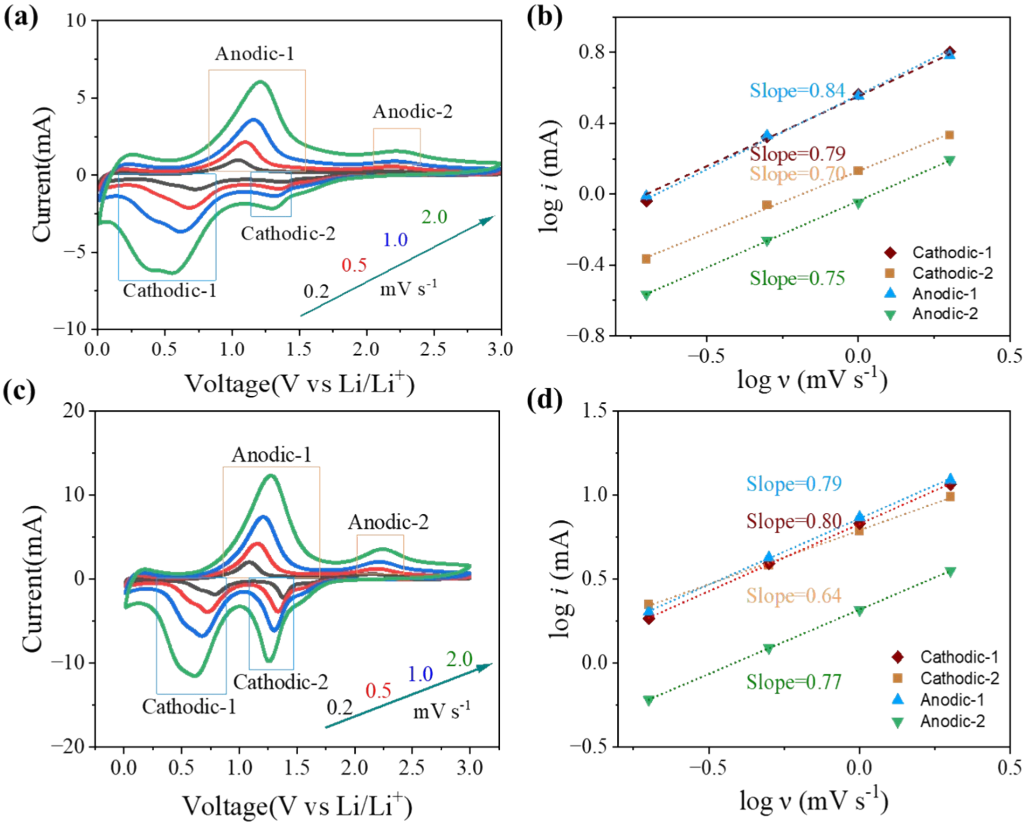

Figure S14. Capacitive contribution of C/SbS_x composites. (a) CV curves at various scan rates from 0.2 to 5.0 mV·s^{-1} of C/SbS_x-MW-1:2; (b) The relation between log(i) and log(ν) of C/SbS_x-MW-1:2. (c) CV curves at various scan rates from 0.2 to 5.0 mV·s^{-1} of C/SbS_x-400°C-1:2; (d) The relation between log(i) and log(ν) of C/SbS_x-400°C-1:2.

As shown in Figure S14a-b, the b values of Cathodic-1, Cathodic-2, Anodic-1, Anodic-2 are 0.70, 0.79, 0.84 and 0.75, respectively. As shown in Figure S14c-d, C/SbS_x-400°C-1:2 also showed high surface-mediated behavior. This implying that capacitance-controlled behavior is an important lithium storage mechanism in C/SbS_x-MW-1:2.

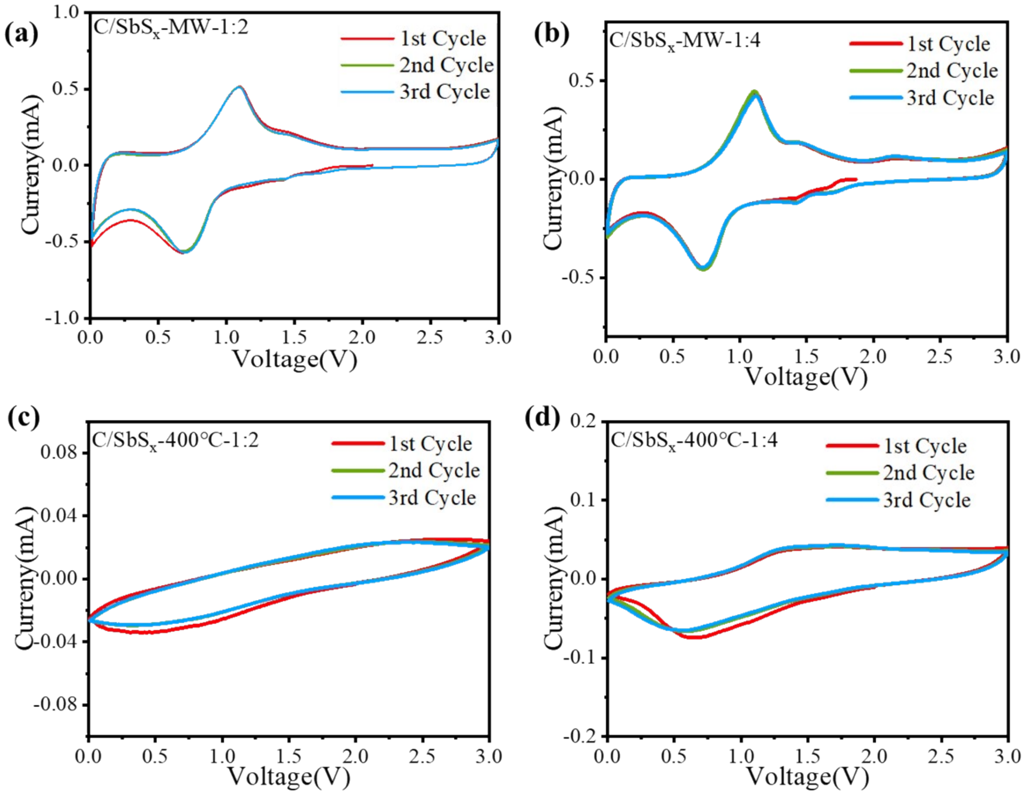

Figure S15. CV curves of amorphous and crystalline C/SbS$_x$ composites after 500 cycles. CV curves of (a) C/SbS$_x$-MW-1:2, (b) C/SbS$_x$-MW-1:4, (c) C/SbS$_x$-400℃-1:2 and (d) C/SbS$_x$-400℃-1:4 at a scan rate of 0.2 mV·S^{-1}.

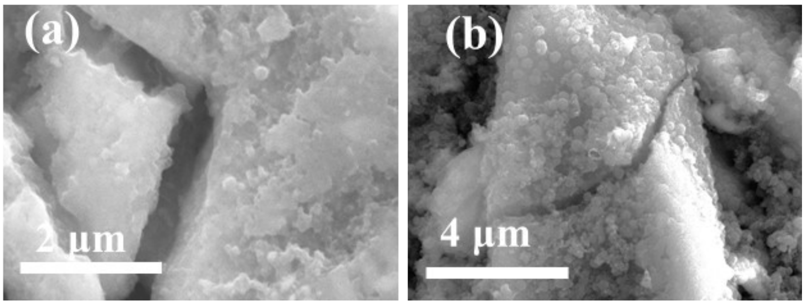

Figure S16. SEM images of C/SbS$_x$-MW-1:2 in delithiated (3.0V) states at (a) 20 cycle and (b) 50 cycle.

TableS1. Electrochemical parameters of the electrodes obtained after fitting and calculation from the measured impedance spectra.

	Pristine C	Pristine Sb_2S_3	C/Sb_2S_3 -1:2	C/SbS_x-MW-1:2	C/SbS_x-MW-1:4
Rs	3.5	5.4	1.8	4.2	3.2
Rf	2.7	8.0	1.9	3.6	3.5
Rct	21.7	45.3	21.1	25.7	18.31

Table S2. Electrochemical performance of Sb_2S_3-based anodes between this work and previous work for LIBs.

Materials	Carbon	Cycle Performance			Rate Performance		References
		Current density ($A\cdot g^{-1}$)	Cycle number	Reversible capacity ($mAhg^{-1}$)	Current density ($A\cdot g^{-1}$)	Reversible capacity ($mAhg^{-1}$)	
Sb_2S_3@C	Porous carbon	0.1	160	745.3	2	187	7
Bundle-like Sb_2S_3		0.1	100	548	1	300.5	8
amorphous Sb_2S_3/C composite	super P	0.1	100	600			9
Sb_2S_3/lotus-pollen composites	Carbide lotus-pollen	0.1	100	591	1	436	10
Sb_2S_3 added bio-carbon	activated cocoanut charcoal	0.1	200	1100	5	431	11
Sb_2S_3 nanorods/porous-carbon	porous-carbon	0.1	150	530.3	2.84	323.6	12
Sb_2S_3/G	graphene	0.19	200	670	1.89	418	13
Amorphous Sb_2S_3		0.19	250	584	5	511	14
Sb_2S_3-graphite nanocomposite	graphite	0.2	250	638.2	1	500	15
rGO-Sb_2S_3-0.5h	graphene oxide	0.25	50	720	2	480	16
Sb_2S_3/Sb		0.4	100	485	1	463	17
VTD Sb_2S_3		0.47	50	749.6	4.73	599.6	6
Sb_2S_3/C	Carbonized glucose	0.5	30	890	4	1019	18
carbon nanotube-in-nanotube@Sb_2S_3	carbon nanotube	1	1500	710	15	361	5
Sb_2S_3/hollow microspheres		1	100	469	5	541	19
MoS_2 decorated Sb@Sb_2S_3@C composites	Carbonization of polypyrrole nanotubes	1	100	760	5	481	20
Amorphous C/SbS_x	charcoal	0.5	500	690	2	512	This work
		0.1	300	726			

Table S3. Synthesis cost of C/SbS_x-MW-1:4 composite and other common commercial anode materials.

Material		Price	proportion	Cost	total cost
C/SbS_x-MW-1:4 (This work)	Industrial Sb_2S_3 (Derived from natural stibnite，98%,325mesh)	7,240-10,035 $/t	0.74	5,358-7,426$	5,628-7,696$/t
	Charcoal(High-temperature treatment)	~580 $/t	0.26	~150$	
	Microwave and ball milling mixing			220$/t	
natural graphite anode	High-end product	8,976 $/t			8,976 $/t
	middle-end product	6,220 $/t			6,220 $/t
	low-end product	4,336 $/t			4,336 $/t
Synthesized graphite anode	High-end product	11,963 $/t			11,963 $/t
	middle-end product	9,679 $/t			9,679 $/t
	low-end product	6,561 $/t			6,561 $/t
Mesophase Carbon MicroBeads		9,788 $/t			9,788 $/t
Synthesized Sb_2S_3		22,140 $/t			22,140 $/t
Commercial Silicon		43,042 $/t			43,042 $/t

Table S4. Electrochemical performance of Sb_2S_3–based anodes between this work and previous work for SIBs.

Materials	Cycle Performance			Rate Performance		References
	Current density	Cycle number	Reversible capacity (mAhg-1)	Current density	Reversible capacity (mAhg^{-1})	
Sb_2S_3@SnS@C	1.0 A g^{-1}	200	442	5.0 A g^{-1}	448	21
Sb_2S_3 nanosheet	0.2 A g^{-1}	100	500	2.0 A g^{-1}	300	22
Sb_2S_3/CS	0.2 A g^{-1}	200	321	0.5 A g^{-1}	423	23
Sb_2S_3/GO	0.2 A g^{-1}	60	463	2.0 A g^{-1}	381	3
Sb_2S_3 added bio-carbon	1.0 A g^{-1}	200	220	2.0 A g^{-1}	208	11
Sn-rGO/Sb_2S_3	0.1 A g^{-1}	100	533	2.0 A g^{-1}	365	24
Sb_2S_3/ppy	0.5 A g^{-1}	50	236	1.0 A g^{-1}	513	25
Sb_2S_3/MoS_2	0.1 A g^{-1}	100	561	2.0 A g^{-1}	507	26
Sb_2S_3 nanowires	0.1 A g^{-1}	50	466	1.0 A g^{-1}	358	27
Sb_2S_3/rGO	0.05 A g^{-1}	50	581	2.0 A g^{-1}	310	28
Sb_2S_3/CNTs	0.05 A g^{-1}	50	412	1.0 A g^{-1}	339	29
Sb_2S_3/P/C	0.05 A g^{-1}	100	611	2.0 A g^{-1}	390	30
ZnS-Sb_2S_3@C	0.1 A g^{-1}	120	630	0.8 A g^{-1}	390	31
This Work	0.1 A g^{-1}	130	510	2.0 A g^{-1}	390	
	1.0 A g^{-1}	1500	251			

Table S5. Electrochemical parameters of the electrodes obtained in SIBs after fitting and calculation from the measured impedance spectra.

	Pristine Sb_2S_3	C/Sb_2S_3 -1:2	C/SbS_x-MW-1:2
Rs	1.0	0.7	1.1
Rf	0.2	0.9	0.4
Rct	25.8	48.6	38.3

References

1. S. Wang, Y. Cheng, H. Xue, W. Liu, Z. Yi, L. Chang and L. Wang, *J. Mater. Chem. A*, 2021, **9**, 7838-7847.
2. P. Ge, L. Zhang, W. Zhao, Y. Yang, W. Sun and X. Ji, *Adv. Funct. Mater.*, 2020, **30**, 1910599.
3. S. Wen, J. Zhao, Y. Zhao, T. Xu and J. Xu, *Chem. Phys. Lett.*, 2019, **716**, 171-176.
4. Y. Cheng, Q. Li, C. Wang, L. Sun, Z. Yi and L. Wang, *Small*, 2017, **13**, 1701993.
5. Z. Y. Yang, Y. F. Yuan, M. Zhu, S. M. Yin, J. P. Cheng and S. Y. Guo, *J. Mater. Chem. A*, 2021, **9**, 22334-22346.
6. Q. Wang, F. Liu, L. Wang, L. Jiang, Q. Wang, B. Hong and Y. Lai, *Scr. Mater.*, 2019, **173**, 75-79.
7. W. Luo, X. Ao, Z. Li, L. Lv, J. Li, G. Hong, Q.-H. Wu and C. Wang, *Electrochimica Acta*, 2018, **290**, 185-192.
8. Z. Yi, Q. Han, Y. Cheng, Y. Wu and L. Wang, *Chem. Commun.*, 2016, **52**, 7691-7694.
9. C.-M. Park, Y. Hwa, N.-E. Sung and H.-J. Sohn, *J. Mater. Chem.*, 2010, **20**, 1097-1102.
10. Q. Ru, X. Chen, B. Wang, Q. Guo, Z. Wang, X. Hou and S. Hu, *Mater. Lett.*, 2017, **198**, 57-60.
11. V. Mullaivananathan and N. Kalaiselvi, *Carbon*, 2019, **144**, 772-780.
12. Q. Wang, Y.-q. Lai, F.-y. Liu, L.-x. Jiang, M. Jia and X.-l. Wang, *Transactions of Nonferrous Metals Society of China*, 2021, **31**, 2051-2061.
13. Y. Dong, S. Yang, Z. Zhang, J.-M. Lee and J. A. Zapien, *Nanoscale*, 2018, **10**, 3159-3165.
14. Q. Wang, Y. Lai, F. Liu, L. Jiang and M. Jia, *Energy Technology*, 2019, **7**, 1900928.
15. Y. Liu, Z. Lu, J. Cui, H. Liu, J. Liu, R. Hu and M. Zhu, *Electrochim. Acta*, 2019, **310**, 26-37.
16. P. V. Prikhodchenko, J. Gun, S. Sladkevich, A. A. Mikhaylov, O. Lev, Y. Y. Tay, S. K. Batabyal and D. Y. W. Yu, *Chem. Mater.*, 2012, **24**, 4750-4757.
17. J. Kong, H. Wei, D. Xia and P. Yu, *Mater. Lett.*, 2016, **179**, 114-117.
18. X. Zhou, L. Bai, J. Yan, S. He and Z. Lei, *Electrochimica Acta*, 2013, **108**, 17-21.
19. J. Xie, L. Liu, J. Xia, Y. Zhang, M. Li, Y. Ouyang, S. Nie and X. Wang, *Nano-Micro Lett.*, 2017, **10**, 12.
20. C. Li, H. Song, C. Mao, H. Peng and G. Li, *J. Alloys Compd.*, 2019, **786**, 169-176.
21. J. Lin, L. Yao, C. Zhang, H. Ding, Yuanhui, Wu, S. Li, J. Han, G. Yue and D. Peng, *ACS Sustainable Chem. Eng.*, 2021, **9**, 11280-11289.
22. S. Yao, J. Cui, Y. Deng, W. G. Chong, J. Wu, M. Ihsan-Ul-Haq, Y.-W. Mai and J.-K. Kim, *Energy Storage Mater.*, 2019, **20**, 36-45.
23. J. Xie, J. Xia, Y. Yuan, L. Liu, Y. Zhang, S. Nie, H. Yan and X. Wang, *J. Power Sources*, 2019, **435**, 226762.
24. S. Bag, A. Roy and S. Mitra, *ChemistrySelect*, 2019, **4**, 6679-6686.
25. T. Zheng, G. Li, L. Zhao and Y. Shen, *Eur. J. Inorg. Chem.*, 2018, **2018**, 1224-1228.
26. Z. Zhang, J. Zhao, M. Xu, H. Wang, Y. Gong and J. Xu, *Nanotechnology*, 2018, **29**, 335401.
27. J. Pan, Z. Zuo, J. Deng, Q. Yao, Z. Wang and H. Zhou, *Surf. Interfaces*, 2018, **10**, 170-175.
28. F. Wu, X. Guo, M. Li and H. Xu, *Ceram. Int.*, 2017, **43**, 6019-6023.
29. J. Li, D. Yan, X. Zhang, S. Hou, D. Li, T. Lu, Y. Yao and L. Pan, *Electrochim. Acta*, 2017, **228**, 436-446.
30. J.-H. Choi, C.-W. Ha, H.-Y. Choi, H.-C. Shin, C.-M. Park, Y.-N. Jo and S.-M. Lee, *Electrochim. Acta*, 2016, **210**, 588-595.
31. S. Dong, C. Li, X. Ge, Z. Li, X. Miao and L. Yin, *ACS Nano*, 2017, **11**, 6474-6482.